World Electric Vehicle Journal

Article

Thermal Analysis of a Flux-Switching Permanent Magnet Machine for Hybrid Electric Vehicles

Wenfei Yu, Zhongze Wu * and Wei Hua

School of Electrical Engineering, Southeast University, Nanjing 210096, China; wenfeiyu@seu.edu.cn (W.Y.)
* Correspondence: zzwu@seu.edu.cn

Abstract: This paper investigates the loss and thermal characteristics of a three-phase 10 kW flux-switching permanent magnet (FSPM) machine, which is used as an integrated starter generator (ISG) for hybrid electric vehicles (HEVs). In this paper, an improved method considering both DC-bias component and minor hysteresis loops in iron flux-density distribution is proposed to calculate core loss more precisely. Then, a lumped parameter thermal network (LPTN) model is constructed to predict transient thermal behavior of the FSPM machine, which takes into consideration various losses as heat sources determined from predictions and experiments. Meanwhile, a simplified one-dimensional (1D) steady heat conduction (1D-SHC) model with two heat sources in cylindrical coordinates is also proposed to predict the thermal behavior. To verify the two methods above, transient and steady thermal analyses of the FSPM machine were performed by computational fluid dynamics (CFD) based on the losses mentioned above. Finally, the predicted results from both LPTN and 1D-SHC were verified by the experiments on a prototyped FSPM machine.

Keywords: flux-switching; permanent magnet; transient thermal analysis; steady thermal analysis; integrated starter generator; lumped parameter thermal network

Citation: Yu, W.; Wu, Z.; Hua, W. Thermal Analysis of a Flux-Switching Permanent Magnet Machine for Hybrid Electric Vehicles. *World Electr. Veh. J.* **2023**, *14*, 130. https://doi.org/10.3390/wevj14050130

Academic Editor: Joeri Van Mierlo

Received: 24 April 2023
Revised: 12 May 2023
Accepted: 17 May 2023
Published: 19 May 2023

1. Introduction

With the energy dilemma and environmental pollution becoming worse, electric-powered vehicles have attracted considerable attention due to their lower green gas emission and oil consumption [1]. Recent hybrid electric vehicles (HEVs) provide long-distance operation due to the optimal match between an engine powered by oil and electric motors powered by electricity stored in batteries. HEVs are widely researched by academics and have become dominant commercial products in EV markets [2,3]. For micro-hybrid EVs, an integrated starter generator (ISG) is the key component of both driving and generating systems, since it plays two major roles, namely, as a starter and a generator. Due to space and weight limitations, the rotor of an ISG is normally directly coupled to the flywheel of the engine in HEVs, where high torque (power) density, large overload torque capability, and high efficiency are expected. Hence, the flux-switching permanent magnet (FSPM) machine is considered as a promising candidate to be applied in electric vehicles, and aerospace and ship propulsion due to its high torque (power) density, high efficiency, and compact structure [4].

With the ever-increasing demand for power (torque) density, research on machine loss and temperature has become a hot topic. An accurate thermal model is an essential tool not only at the machine design stage but also for online prediction of temperature distribution [5]. While finite element method (FEM)-based and computational fluid dynamics (CFD)-based thermal models can achieve high accuracy, a lumped parameter thermal network (LPTN)-based model is often preferred thanks to its lower computational requirement and good accuracy [6–8].

In [9], the thermal influence of vehicle integration on the thermal load of an ISG was discussed by a FEM-based thermal model. In [10], an axially segmented FEM model of

a FSPM machine was proposed to analyze the coupled electromagnetic–thermal performances. A thermal resistance network was established based on a nine-node model for an interior PM (IPM) machine and the transient temperature characteristics were obtained [11]. In [12], a numerical approach for estimation of convective heat transfer coefficient in the end region of an ISG was proposed, and both the local and averaged heat transfer coefficients were estimated. A systematic procedure to study the impact of each thermal phenomenon in IPM machines used for ISG was presented in [13]. In [14], a reduced model in a multi-physical electric machine optimization procedure was proposed.

The contribution of this paper is to propose two temperature prediction models for a 10 kW FSPM machine as an ISG for micro-hybrid vehicles; namely, a LPTN thermal model, and a one-dimensional (1D) steady heat conduction (SHC) (1D-SHC) model. The two methods can both quickly predict the internal temperature distribution of the FSPM machine. The results were verified by CFD and experiments to prove their accuracy.

Section 2 will propose an improved core loss model considering both the DC-bias component and minor hysteresis loops in iron flux-density, and the core loss of the FSPM machine is calculated and verified by experiments. Then, in Section 3 a LPTN model is proposed firstly to predict transient thermal behavior. After that, a simplified 1D-SHC thermal model is proposed to reveal the relationship between design parameters of a cooling jacket and thermal distribution of stator, and verified by experiments under different cooling conditions. In Section 4, both steady and transient thermal predictions are compared with those from ANSYS fluent-based CFD. Experiments with rising temperatures were conducted on a prototyped FSPM machine and are detailed in Section 5, followed by conclusions in Section 6.

2. Loss Prediction Model

The key dimensions of the studied FSPM machine are listed in Table 1. In addition to electromagnetic parameters, the thermal conductivities, the specific heats, and densities of materials used for transient thermal analysis are presented in Table 2. The employed PM material was N35 and the silicon steel sheet was 35WW310.

Table 1. Design specifications of the FSPM machine.

Parameter	Symbol	Value	Unit
DC-link voltage	U_{DC}	144	V
Phase number	m	3	-
Stator slots	N_s	12	-
Rotor pole pairs	N_r	10	-
PM pole pairs	N_{PM}	6	-
Rated power	P_N	10	kW
Rated speed	n_N	1000	r/min
Rated torque	T_N	95.5	Nm
Stator outer diameter	D_{so}	260	mm
Rotor inner diameter	D_{ri}	50	mm
Air-gap length	g_0	0.9	mm
Stack length	L_a	55	mm

Table 2. Thermal conductivities of materials.

Materials	Thermal Conductivity (W/m/°C)	Specific Heat Capacity (J/kg/°C)	Density (kg/m^3)
Steel silicon	23	460	7650
Copper	380	385	8978
PM	9	504	7500
Aluminum	237	833	2688
Air	0.02624	1005	1.205

The loss of the FSPM machine includes winding joule loss, core loss, eddy current loss in PMs, housing and frictional loss, and excess loss. According to the Bertotti G. model [15], the core loss of PM machines P_{Fe} consists of hysteresis loss, eddy current loss and excess loss, and the core loss yields:

$$P_{Fe} = P_h + P_c + P_e = k_h f B_m^{\alpha} + k_c f^{1.5} B_m^{1.5} + k_e f^2 B_m^2 \quad (1)$$

where *Ph* is hysteresis loss in W, *Pc* is the classical eddy current loss in W, P_e is the excess loss in W, k_h, k_c, and k_e are the corresponding coefficient of the above losses, respectively, f is the fundamental frequency of a magnetizing flux in Hz, and B_m is the maximum flux density in core in T.

However, Equation (1) only works given a purely sinusoidal magnetizing flux. To exactly obtain the magnetizing flux-density characteristics in the FSPM machine core, eight key points located in stator and rotor respectively are selected, as shown in Figure 1a. Correspondingly, the resultant loci of the flux-density radial and tangential components (B_{gr}/B_{gt}) are predicted, as shown in Figure 1b. Clearly, for the stator points 1 and 2, the surrounded areas by the B_{gr}/B_{gt} loci are to be almost zero, which means the averaged B_{gr}/B_{gt} values are nearly zero. However, for points 3 and 4, the corresponding areas (the blue one and the pink one) are not centrosymmetric, which means a DC-biased component exists. For the points 5~8 in the rotor, the B_{gr}/B_{gt} loci are all centrosymmetric and the averaged values are close to zero. A typically DC-biased component and a minor hysteresis loop are shown in Figure 1c,d, respectively.

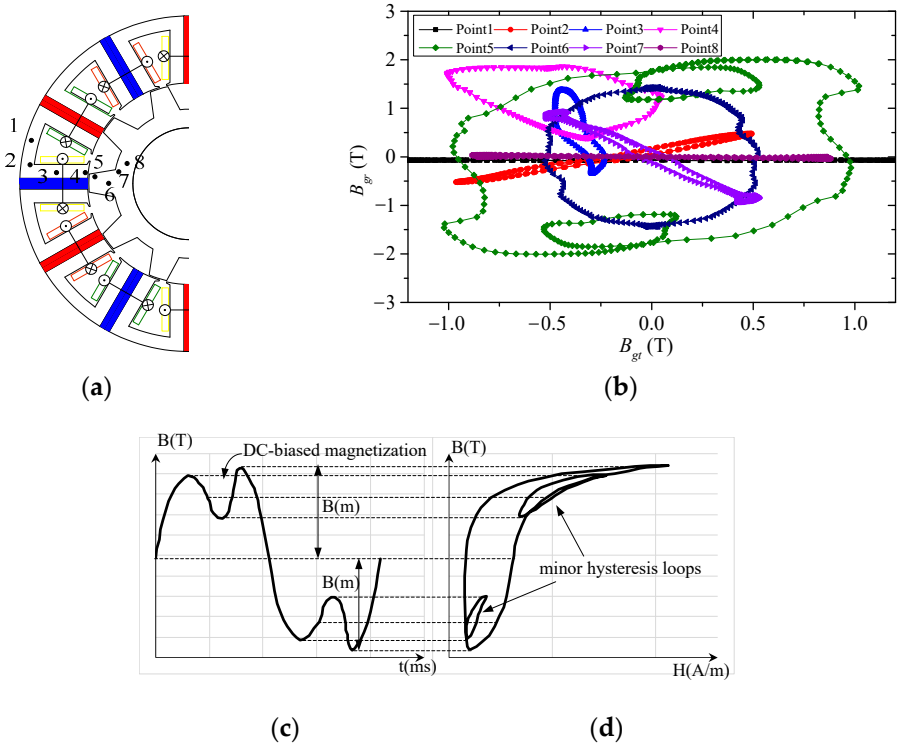

Figure 1. The flux-density loci of key points in the FSPM machine. (**a**) The key stator and/rotor core points in the FSPM machine. (**b**) The B_{gr}/B_{gt} loci of key stator and rotor core points. (**c**) The DC-biased components of B_{gr}/B_{gt}. (**d**) The local minor hysteresis loop.

Unfortunately, the influence of magnetized DC-biased components and minor hysteresis loops are not well recognized in the commercial FEM software packages [16]. Hence, to predict the core loss of FSPM machines more precisely, an improved model considering both DC-biased component and minor hysteresis loops is proposed as follows. Assuming that the minor loop is similar to the major loop, the core loss can be divided into radial and

tangential components. The total core loss, including the hysteresis loss [17], eddy current loss [18], and excess loss [19], can be obtained as follows:

$$P_h = k_h f L_a \sum_{i=1}^{N_{elem}} \Delta A_i \left[\left(\sum_{j=1}^{N_{pr}^i} {B_{rm}^{ij}}^2 \right) \varepsilon(\Delta B_r) + \left(\sum_{j=1}^{N_{pt}^i} {B_{tm}^{ij}}^2 \right) \varepsilon(\Delta B_t) \right] \quad (2)$$

$$P_c = \frac{K_c}{2\pi^2} \frac{L_a}{N_{setp}} \cdot \sum_{k=1}^{N_{step}} \sum_{i=1}^{N_{elem}} \Delta A_i \left[\left(\frac{B_{rmi}^{k+1} - B_{rmi}^k}{\Delta t} \right)^2 + \left(\frac{B_{tmi}^{k+1} - B_{tmi}^k}{\Delta t} \right)^2 \right] \quad (3)$$

$$P_e = \frac{K_e L_a}{N_{setp}} \sum_{k=1}^{N_{step}} \sum_{i=1}^{N_{elem}} \Delta A_i \left[\left(\frac{B_{rmi}^{k+1} - B_{rmi}^k}{\Delta t} \right)^{1.5} + \left(\frac{B_{tmi}^{k+1} - B_{tmi}^k}{\Delta t} \right)^{1.5} \right] \quad (4)$$

$$P_{Fe} = P_h + P_c + P_e \quad (5)$$

where N_{elem} is the finite elements number, ΔA_i is the ith finite element area in m^2, ${N_{pr}}^i$ and ${N_{pt}}^i$ are the radial and tangential minor loops numbers of the ith element during one period, respectively, N_{step} is the calculation steps number, ${B_{rm}}^{ij}$ and ${B_{tm}}^{ij}$ are the maximum radial and tangential flux-densities of the jth hysteresis loop in the ith element in T, respectively, ${B_{rmi}}^k$ and ${B_{tmi}}^k$ are the maximum radial and tangential flux-density of the ith element in the kth calculation step in T, and Δt is the time step in s.

According to Equations (2)–(5), the core loss can be obtained by a combination platform of ANSYS and MATLAB, where based on ANSYS the detailed B_{gr}/B_{gt} results of each meshed iron element can be acquired, and based on MATLAB the core loss versus rotating speeds under different conditions can be assessed by a series of data processing calculations according to Equations (2)–(5). The no-load core loss density distribution of the stator and rotor is shown in Figure 2. Consequently, the predicted core losses versus rotor speed are compared with those obtained by commercial software, e.g., by JMAG and ANSYS EM as shown in Figure 3. It can be seen that the core losses obtained by the improved method are slightly higher than those from software, which validates the influence of the DC-biased component and minor hysteresis loop, and also validates the feasibility of the improved core loss prediction method.

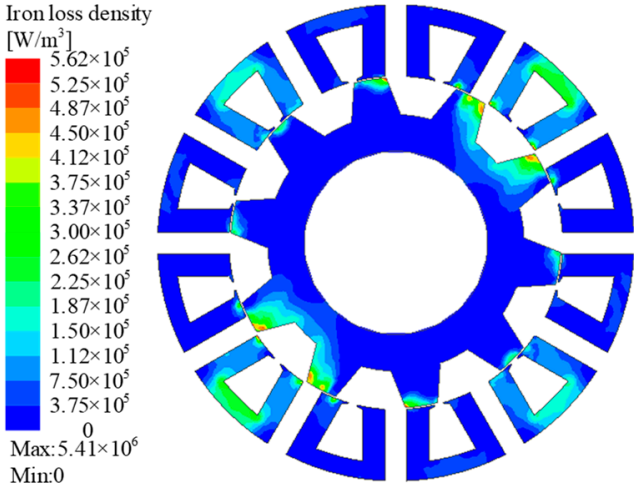

Figure 2. No-load core loss density distribution of the machine (n = 1000 r/min).

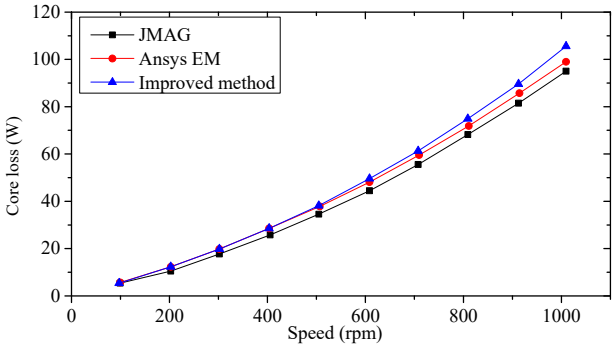

Figure 3. No-load core loss versus speed of the FSPM machine by three methods.

In addition, the no-load eddy current density distribution derived by 3D-FEM is shown in Figure 4. The resulting no-load eddy loss in PMs P_{pmc} and housing P_{hc} versus rotating speeds are shown in Figure 5. It can be found that with the increase of the speed, the eddy current losses in PMs and housing increase gradually, which is caused by the air-gap harmonic fields and can be calculated by Equation (6) [20],

$$P_{eddy} = \frac{1}{T}\int_{t_c}\sum_{i=1}^{k} J_e^2 \Delta_{Ai} \sigma_r^{-1} L_a dt \tag{6}$$

where P_{eddy} is the eddy current loss in PM and housing in W, J_e is the current density in each element in A/m^2, Δ_{Ai} is the ith element area in m^2, σ_r is the conductivity of the eddy current zone in S/m, and t_c is the time corresponding to a period in each element in s.

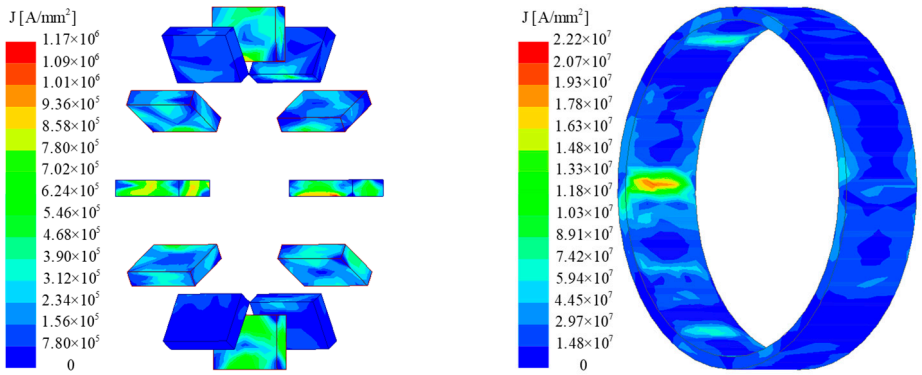

(**a**) (**b**)

Figure 4. No-load 3D eddy current density distribution @1000 r/min. (**a**) PMs; (**b**) housing.

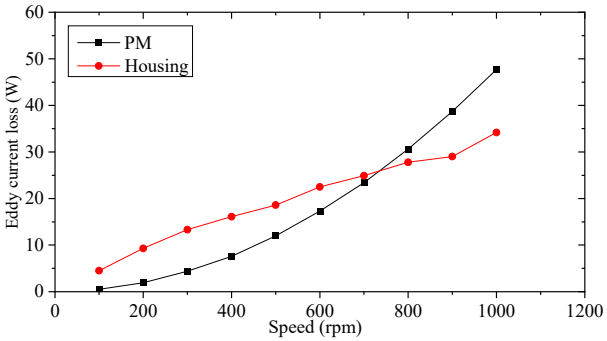

Figure 5. No-load eddy current losses in PMs and housing versus rotating speeds.

The frictional loss P_{fri} of the FSPM machine yields [21]:

$$P_{fri} = 16N_r\left(\frac{v_r}{40}\right)^3\sqrt{\frac{L_a}{19}\times 10^3} \tag{7}$$

where v_r is the rotor peripheral speed in m/s. It is found that P_{fri} = 10.7 W under the rated speed of 1000 r/min.

Finally, a no-load test under different rotation speeds is conducted on a prototyped FSPM machine to verify the predicted results, where the machine is controlled by a DSP-based controller and the input power is obtained by a power analyzer. The frictional loss is so small that it can be neglected. Therefore, the input power is equal to the total loss. The total losses versus rotor speeds by different methods are compared in Figure 6. Compared with the results obtained by commercial software, the predicted core losses derived by the improved method agree with the measurements with the smallest deviations.

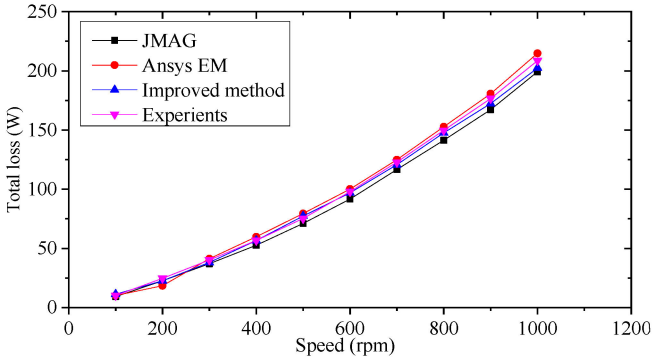

Figure 6. Total loss versus speed by different prediction methods and experiments.

3. Two Thermal Models

For the prototyped FSPM machine, a circumferential water jacket with one cooling duct is introduced in the stator housing as shown in Figure 7. The coolant channel of the casing adopts a single-layer water jacket cooling structure. Figure 7a shows the schematic diagram of the FSPM machine structure. Figure 7b–d show the housing, coolant flow path, and machine assembly, respectively. Figure 7b shows the cross-sectional diagram of the machine, and Figure 7c shows the cross-sectional diagram of the cooling duct. Arrows are used in Figure 7c to indicate the flow path of the coolant. The blue arrow represents the low temperature coolant near the inlet, while the red arrow represents the coolant that has been heated through heat exchange. The fluid running inside the cooling duct can be modeled as the movement of fluid in a rectangular channel using dimensionless numbers. Consequently, the convection coefficient can be obtained in the following stages.

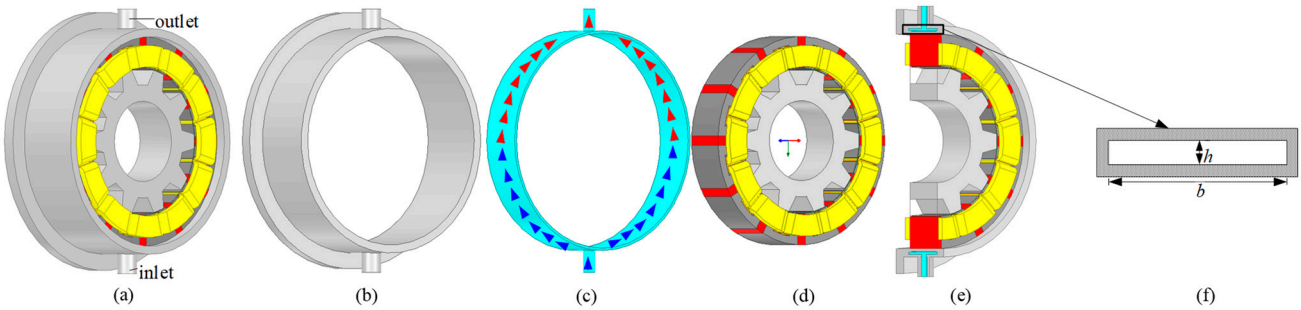

Figure 7. The cooling system of the FSPM machine. (**a**) FSPM machine structure, (**b**) housing, (**c**) coolant flow path, and (**d**) machine assembly. (**e**) Cross-section of the cooling jacket, and (**f**) schematic diagram of cooling duct.

Firstly, with the cooling jacket cross-section in Figure 7c, the Prandtl number of the fluid P_{rf} yields

$$P_{rf} = \frac{c_f \eta_f}{\lambda_f} \tag{8}$$

where c_f is the specific heat capacity of fluid in J/(kg·°C), η_f is fluid dynamic viscosity in N·s/m^2, and λ_f is the fluid thermal conductivity in W/(m·°C).

Secondly, the Reynolds number of fluid R_e yields

$$R_e = \frac{v d_e}{v_f} \tag{9}$$

where v is the velocity of fluid in m/s, v_f is the fluid kinetic viscosity in m^2/s, and d_e is the hydraulic radius in m by Equation (10).

$$d_e = \frac{4A_{cs}}{s} = \frac{4bh}{2(b+h)} \tag{10}$$

where A_{cs} is a cross-section area of a single cooling duct in m^2. s, b, and h are the wetted perimeter, width, and height of cooling duct in m, respectively.

Approximately, in a circumferential cooling duct, the velocity of fluid can be figured out as

$$v = \frac{Q}{A_{cs}} \tag{11}$$

where Q is the fluid quantity in kg/s.

According to the value of Re, the fluid flow can be divided into turbulence flow and laminar flow. The Nusselt number of the laminar flow N_{ufl} yields [22],

$$Nu_{f1} = 0.644 (Re^{0.5}) {P_{rf}}^{\frac{1}{3}} \tag{12}$$

For turbulence flow, the Nusselt number N_{uft} yields

$$Nu_{ft} = 0.023 \left(Re^{0.8} \right) {P_{rf}}^{0.4} \left(\frac{\eta_f}{\eta_w} \right)^{0.14} \tag{13}$$

where η_w is the dynamic viscosity of housing in N·s/m^2.

Based on the similarity criterion of fluid [22], the convection heat transfer coefficient h_{f0} yields

$$h_{f0} = \frac{Nu_f \lambda_f}{d_e} \tag{14}$$

Considering that turbulence flow shows a better heat dissipation than laminar flow, the former is employed in the cooling jacket, where the convection heat transfer coefficient h_f of the cooling jacket is affected by the geometric parameters and the velocity of the fluid, and can be given by

$$h_f = \lambda_f \frac{b+h}{2bh} \left(\frac{2Q}{v_f (b+h)} \right)^{0.8} {P_r}_f^{0.4} \left(\frac{\eta_f}{\eta_w} \right)^{0.14} \tag{15}$$

From Equation (15), when the fluid quantity keeps constant, as the cross-sectional area of the cooling ducts decreases, the convection coefficient of the cooling jacket increases. However, a small cross-section cooling duct is not only difficult to manufacture, but also may lead to high inlet velocity and high hydraulic pressure, which causes the corrosion of cooling duct and deteriorates the operation stability. In the following, two thermal models are proposed, one a LPTN model and the other a 1D-SHC model.

3.1. Lumped Parameter Thermal Network Model

A LPTN model enables the heat flow and the temperature distribution inside the machine by means of an equivalent thermal circuit, which is composed of heat sources, thermal resistances, and thermal capacitances. For the convenience of calculation and improved accuracy, three assumptions are made as follows [23–25]:

1. Symmetrical temperature distribution and the same cooling conditions along the circumference;
2. Uniformly distributed thermal capacity and heat generation;
3. Independent heat flow in radial and axial directions

To simplify the calculation load, only 1/24 of the FSPM machine is modeled as shown in Figure 8 due to symmetry, where the heat sources including stator/rotor core losses, PM/housing eddy current losses, and windings joule loss are considered. The thermal resistances and capacitances can be determined according to the machine geometry and the physical properties of materials. Tables 3 and 4 list the corresponding resistances and capacitances of the LPTN model. A preliminary selection of the resistances and capacitances can be determined according to the machine geometry and physical properties of the materials used [26].

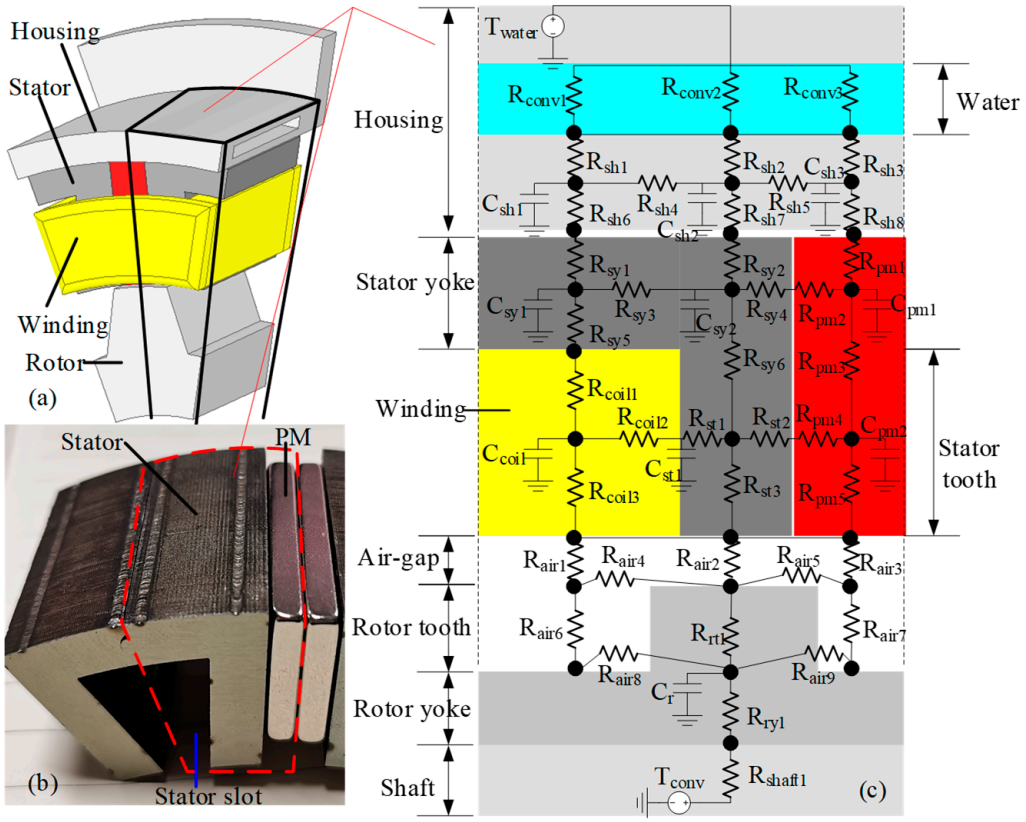

Figure 8. The LPTN model of the FSPM machine: (**a**) 3D module structure; (**b**) stator module; (**c**) the LPTN model of the 1/24 FSPM machine.

Table 3. Component thermal resistances of the LPTN model.

Thermal Resistances	Value (°C/W)	Thermal Resistances	Value (°C/W)
R_{sh1}, R_{sh2}, R_{sh3}	0.0004307	R_{st1}, R_{st2}	0.1479
R_{sh4}	0.1094	R_{st3}	0.01449
R_{sh5}	0.07664	R_{coil1}	0.6297
R_{sh6}, R_{sh7}, R_{sh8}	0.0004469	R_{coil2}	4.895
R_{sy1}, R_{sy2}	0.00359	R_{coil3}	0.7244
R_{sy3}	0.2107	R_{pm1}	0.01197
R_{sy4}	0.1128	R_{pm2}	0.04699
R_{sy5}	0.003729	R_{pm3}	0.05441
R_{sy6}	0.01632	R_{pm4}	0.2054
R_{air1}, R_{air2}, R_{air3}	1.096	R_{pm5}	0.04829
R_{air4}, R_{air5}	596	R_{rt1}	0.02435
R_{air6}, R_{air7}	27.84	R_{ry1}	0.03246
R_{air8}	30.76	R_{shaft1}	0.2613
R_{air9}	56.14	-	-

Table 4. Thermal capacitances of the LPTN model.

Thermal Capacitance	Value (J/°C)	Thermal Capacitance	Value (J/°C)
C_{sh1}	30.82	C_{st1}	71.37
C_{sh2}	21.86	C_{coil1}	0.0036
C_{sh3}	10.75	C_{pm1}	10.67
C_{sy1}	31.63	C_{pm2}	33.14
C_{sy2}	22.98	C_r	497.2

With the convection heat transfer coefficient, the thermal resistance R_{convi} (i = 1, 2, 3) representing the heat dissipation by cooling medium convection between the housing external surface and ambient can be calculated by Equation (16) [25],

$$R_{convi} = \frac{1}{h_{convi} A_{convi}} \tag{16}$$

where R_{convi} is the thermal resistance due to convection heat transfer in °C/W, h_{convi} is the convection heat transfer coefficient in W/(m^2·°C), and A_{convi} is the convective area in m^2. Here, the area of the end-part winding is considered.

Since the heat exchange between stator and rotor through the air-gap is assumed to be only by convection, Equation (16) is also used for the calculation of the thermal resistances R_{airi}.

In addition to heat convection, heat conduction is also an important way for heat dissipation. The resistance representing the heat flow in the radial direction is modeled by using Equation (17),

$$R_{radial} = \frac{ln(r_o/r_i)}{2\pi\lambda L} \tag{17}$$

where r_o and r_i are the outer and inner diameter of the cylinder in m, λ is the thermal conductivity of the material in W/m/°C, and L is the cylinder length in m.

In the tangential direction, the thermal resistance due to conduction heat transfer is given by,

$$R_{tangential} = \frac{l}{\lambda A_{cond}} \tag{18}$$

where l is a portion length of the path considered in m, and A_{cond} is the area for the conduction in m^2.

Figure 8a,b show the 3D module structure and modular stator element of the FSPM machine. Based on the thermal resistances above, a thermal resistance network of the 1/24 machine is constructed as shown in Figure 8c, where R_{sh1}-R_{sh8}, R_{sy1}-R_{sy6}, R_{air1}-R_{air9},

R_{st1}-R_{st3}, R_{coil1}-R_{coil3}, and R_{pm1}-R_{pm5} represent the thermal resistances of the housing, stator yoke, air-gap, stator tooth, stator winding coils, and PMs. R_{rt1}, R_{ry1}, and R_{shaft1} represent the thermal resistances of rotor tooth, rotor yoke, and shaft, respectively. C_{sh1}-C_{sh3}, C_{sy1}-C_{sy2}, C_{st1}, C_{coil1}, C_{pm1}-C_{pm2}, and C_{rt} represent the thermal capacitances of the housing, stator yoke, stator tooth, winding coils, PMs, and rotor tooth. Here, since the heat dissipated by forced convection is much larger than that by radiation, the radiation heat dissipation is ignored.

Under two typical operation conditions, i.e., the speed of 1000 r/min and the phase current of 30.7 A (RMS) and 60 A (RMS), the transient temperature rises of different components under forced water cooling are obtained by the LPTN model, and the results are shown in Figure 9. It takes around 70 min for the machine under water cooling to reach a thermal steady state where the armature windings have the highest temperatures (45.7 °C@30.7 A and 82.8 °C@60 A under water cooling). In addition, since the PMs are mounted on the stator, the temperature of the PMs is very close to that of the stator core, exhibiting the advantage of FSPM machines.

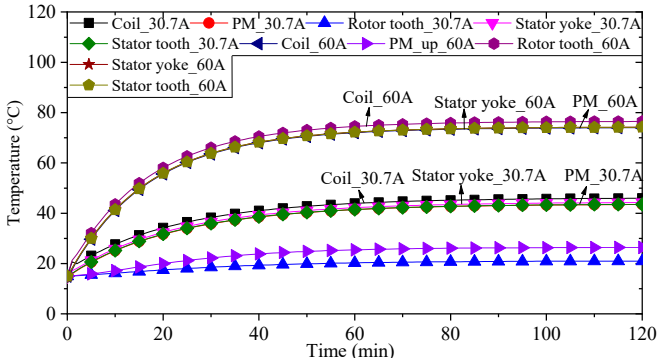

Figure 9. The predicted temperature rises by the LPTN model under water-cooling conditions @ nN = 1000 r/min and Iph = 30.7 A and 60 A (RMS).

3.2. One-Dimensional Steady Heat Conduction Model

Generally, LPTN and FEM have been widely employed in thermal analysis of electrical machines. However, these two methods are normally time-consuming and require complicated modeling. For water-cooling machines, in order to select a reasonable flow rate of coolant, a 1D-SHC approach is proposed based on heat transfer and fluid mechanics as shown in Figure 10, and the relationship between the internal temperature of the stator and the coolant flow rate and coolant temperature is obtained.

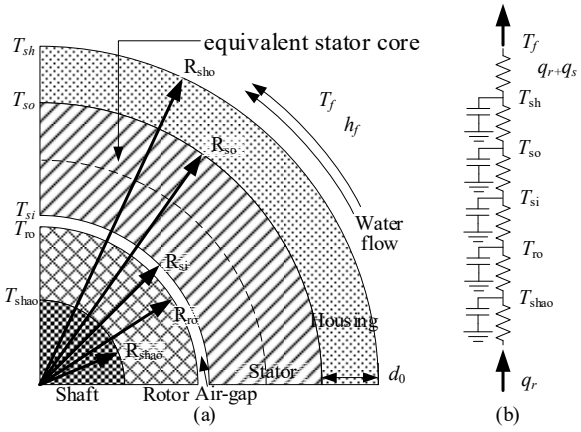

Figure 10. One-dimensional steady heat conduction model of the FSPM machine. (**a**) Equivalent heat conduction model; (**b**) equivalent heat flow path.

It should be noted that the 1D-SHC model is based on the following assumptions. (1) The loss is uniformly distributed in each component of the machine. (2) The heat generated by joule loss and stator core loss is only dissipated by the housing. (3) The stator laminations, windings, and PMs are simplified to a homogeneous heating unit and the equivalent averaged thermal conductivity λ_{avg} yields [26,27]:

$$\lambda_{ave} = \frac{A_s + A_{wind} + A_{pm}}{\frac{A_s}{\lambda_s} + \frac{A_{wind}}{\lambda_{cu}} + \frac{A_{pm}}{\lambda_{pm}}} \tag{19}$$

where A_s, A_{wind}, and A_{pm} are the cross-section area of the stator, windings, and PMs in m^2, respectively, λ_s, λ_{wind}, and λ_{pm} are the thermal conductivity of stator, windings, and PMs in W/(m·°C).

The winding and insulation layering is used to calculate the thermal conductivity of the stator windings. Figure 11 shows the equivalent diagram of the winding structure, where the insulation and windings are arranged with intervals. The slot filling factor is set as 0.35 according to the prototyped machine. The equivalent winding thermal conductivity yields:

$$\lambda_{wind} = \sum_{i=1}^{n} \delta_i / \sum_{i=1}^{n} \frac{\delta_i}{\lambda_i} \tag{20}$$

where δ_I is the thickness of the ith layer in m, λ_i is the thermal conductivity of the ith layer in W/(m·°C).

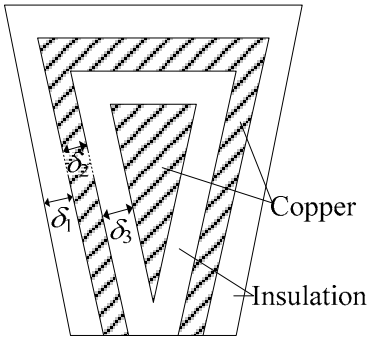

Figure 11. Equivalent diagram of the winding structure.

Then, the equivalent volumetric heat generation of stator q_{Vs} and rotor q_{Vr} can be obtained by

$$\begin{cases} P_{eave} = \frac{P_s V_s + P_{cu} V_{cu} + P_{pm} V_{pm}}{V_s + V_{cu} + V_{pm}} \\ q_{Vs} = \frac{P_{eave}}{V_{equ}} \\ q_{Vr} = \frac{P_r}{V_r} \end{cases} \tag{21}$$

where P_{eave} is equivalent average loss in W, P_s, P_{cu}, P_{pm}, and P_r are the stator core loss, winding joule loss, eddy current loss in PMs, and rotor core loss in W, respectively, V_s, V_{cu}, V_{pm}, V_{equ}, and V_r are the volume of stator, winding, PM, equivalent stator, and rotor in m^3, respectively.

Since the thermal model is simplified into a 1D-SHC model, the heat flux density of stator/rotor (q_s/q_r) yields

$$\begin{cases} q_s = q_{Vs}/S_s \\ q_r = q_{Vr}/S_r \end{cases} \tag{22}$$

where S_s/S_r is the cross-section area of stator/rotor lamination in m^2.

The inlet and outlet temperature of the cooling fluid can be detected by a hand-held infrared thermometer. Thus, the temperature of the fluid T_f equals

$$T_f = \frac{T_i + T_o}{2} \tag{23}$$

where *Ti*/*To* is the inlet/outlet temperature of the fluid in °C.

According to the 1D thermal circuit in Figure 10b, the temperature of housing T_{sh} can be derived by

$$T_{sh} = T_f + \frac{q_r}{\pi h_f (R_{sho} - R_{shao})} + \frac{q_s}{\pi h_f (R_{sho} - R_{si})} \tag{24}$$

where *hf* is the fluid convection coefficient in W/(m^2·K), *Rsho* is the housing outer radius in m, *Rshao* is the shaft outer radius in m, and *Rsi* is the stator inner radius in m.

The temperature of stator yoke T_{sy} yields

$$T_{sy} = T_{sh} + (q_r + q_s)\frac{ln(R_{sho}/R_{so})}{2\pi h_{sh}} \tag{25}$$

where R_{so} is the stator outer radius in m, and h_{sh} is the housing thermal conductivity in W/(m·°C).

The differential equations of the heat conduction and the boundary conditions for a cylinder with uniform heat generation are as follows [23]:

$$\begin{cases} \frac{1}{r} \cdot \frac{d}{dr}\left(r \cdot \frac{dt}{dr}\right) + \frac{q_r}{\lambda_r} + \frac{q_r + q_s}{\lambda_{avg}} = 0 \\ T = T_{sy}, r = R_{so}; \frac{dt}{dr} = 0, r = 0 \end{cases} \tag{26}$$

where λ_r is the rotor thermal conductivity in W/(m·°C).

The thermal distribution of the machine can be given by

$$\begin{cases} h_f = \lambda_f \frac{b+h}{2bh}\left(\frac{2v}{v_f}\right)^{0.8} Pr_f^{0.4}\left(\frac{\eta_f}{\eta_w}\right)^{0.14} \\ T(r) = \frac{{R_{so}}^2}{4}\left(\frac{q_r}{\lambda_r} + \frac{q_r + q_s}{\lambda_{avg}}\right) \end{cases} \tag{27}$$

Hence, the stator teeth temperature can be obtained by

$$\begin{aligned} T_{st} = \tfrac{T_i + T_o}{2} + (q_r + q_s)\left(\tfrac{ln(R_{sho}/R_{so})}{2\pi h_{sh}} + \tfrac{{R_{so}}^2 - {R_{si}}^2}{4\lambda_{avg}}\right) + \\ \tfrac{1}{\pi h_f}\left(\tfrac{q_r}{R_{sho} - R_{shao}} + \tfrac{q_s}{R_{sho} - R_{si}}\right) + \tfrac{\left({R_{so}}^2 - {R_{si}}^2\right) q_r}{4\lambda_r} \end{aligned} \tag{28}$$

According to Equations (11), (15) and (28), as the average velocity of fluid increases, the convection coefficient of the cooling jacket increases and the stator temperature decreases. According to the prototype dimensions, when the no-load machine is running at the speed of 1000 r/min, the relationship between the temperature of the equivalent stator core (marked in Figure 10) and the inlet velocity can be obtained as shown in Figure 12. Obviously, as the inlet velocity of water increases to 0.6 m/s, the equivalent stator core temperature decreases almost linearly. When the inlet velocity increases to 1 m/s, the stator core temperature varies nonlinearly and slowly, so 1 m/s is set as the rated cooling inlet velocity of the FSPM machine, corresponding to a pump flow of 1800 L/h.

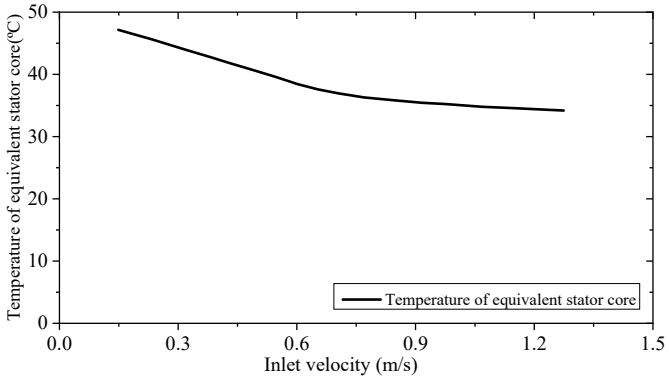

Figure 12. The temperature of equivalent stator core vs. inlet velocity by 1D-SHC.

4. CFD-Based 3D Temperature Field Verification

In order to verify the proposed LPTN and 1D-SHC models, based on the loss calculated by FEM, a 3D-CFD thermal model is built as shown in Figure 13a. Figure 13b corresponds to water cooling.

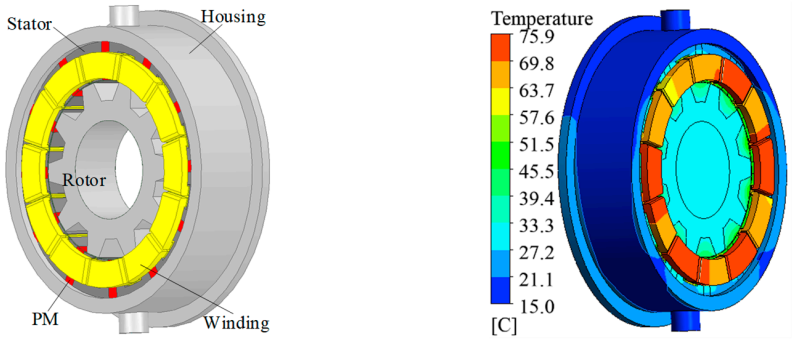

Figure 13. Three-dimensional CFD thermal model of the FSPM machine and steady-state temperatures @30.7 A and 60 A; (**a**) 3D-CFD thermal model; (**b**) water cooling.

When the cooling jacket is injected with an total inlet flow of 1800 L/h, a phase current of 30.7 A and 60 A, as well as a speed of 1000 r/min, the transient temperature rises of different components under forced water cooling are obtained as shown in Figure 14. It can be seen that the armature windings achieve the highest temperature under forced water-cooling conditions, whereas the armature windings temperature difference is 31 °C when the armature current is 30.7 A and 60 A, respectively. In addition, compared with the results obtained by the LPTN model shown in Figure 9, both the steady-state and transient results agree well.

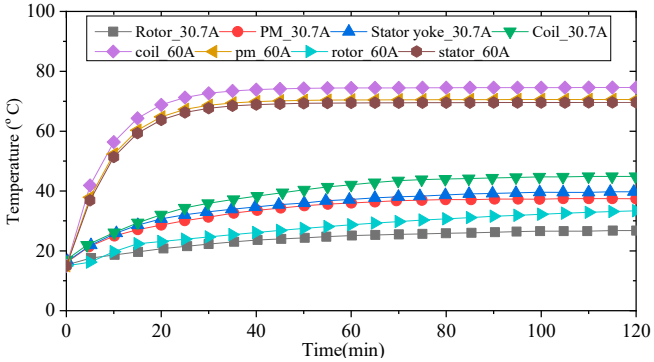

Figure 14. The 3D-CFD predicted temperature rises of different components of the FSPM machine.

On the other hand, to verify the 1D-SHC model, the predicted equivalent stator core temperatures vs. inlet velocity by 1D-SHC and CFD are compared in Figure 15, where the operation status and cooling conditions are consistent with the 1D-SHC model. In addition to predicted temperatures, the time consumed by the three methods is compared in Table 5. Obviously, both the LTPN and 1D-SHC methods can save considerable time, which is favorable for the optimal design of machines.

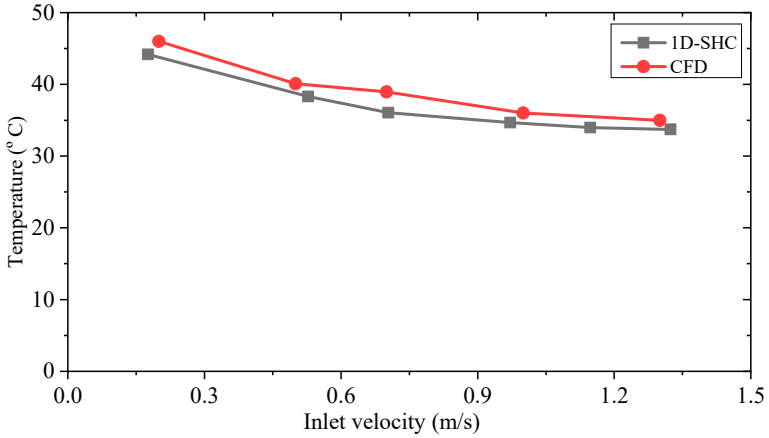

Figure 15. The predicted equivalent stator core temperatures vs. inlet velocity by 1D-SHC and CFD.

Table 5. Comparison of time consumed by temperature prediction methods.

Temperature Prediction Methods	Steady State	Transient
LPTN method	2 s	7 s
1D-SHC method	0.6 s	1.4 s
CFD method	11 min	100 min

5. Experiment Verification

To validate the proposed thermal prediction models, a prototyped FSPM machine was manufactured and tested as shown in Figure 16. The prototyped FSPM machine was driven by an inverter supplied by a DC power source and the output shaft was directly connected with a dynamometer machine, in which a torque transducer and a resolver were equipped to measure torque and (rotor position) speed, respectively. Figure 17 compares the FEA-predicted and experimental results of torque versus phase currents. It can be seen that good agreements can be achieved with a deviation below 8%.

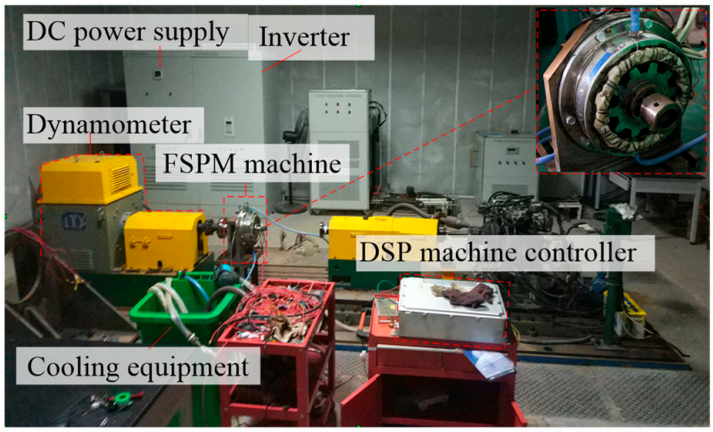

Figure 16. Prototype photographs and test platform.

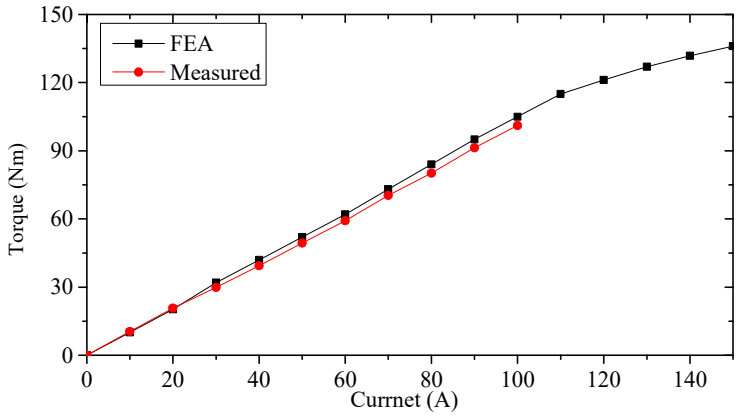

Figure 17. FEA-predicted and experimental torque versus phase currents.

To verify the LPTN model, experiments on transient temperature rise were performed. Under the phase current of 30.7 A and rated speed of 1000 r/min, the transient temperature rises of different components under forced water cooling were obtained as shown in Figure 18, where the temperature was detected with a hand-held infrared thermometer. Under forced water-cooling conditions, the measured highest temperature was 47.1 °C. Compared with the results obtained by LPTN (Figure 9) and CFD (Figure 14), it was found that the steady-state and transient results of the three methods were very close. Figure 19 shows the experimental steady-state temperatures under forced water cooling. Obviously, agreement between the experiments and LPTN was achieved, validating the effectiveness of the LPTN model.

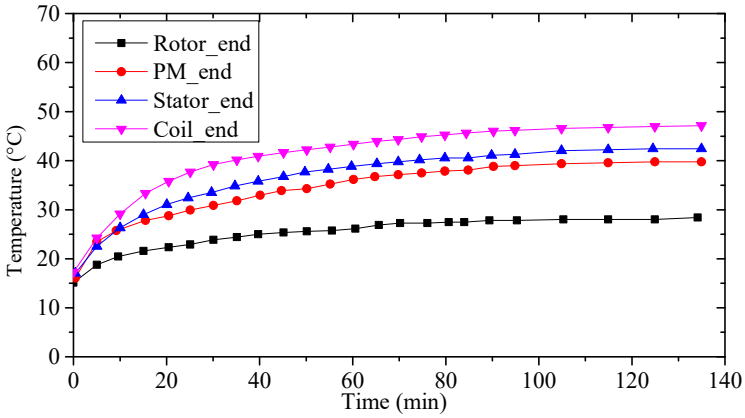

Figure 18. The temperature rises of the FSPM machine under forced water-cooling conditions.

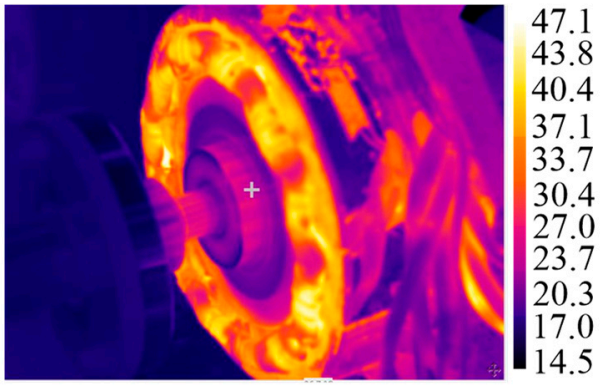

Figure 19. Steady-state temperature distribution of the FSPM machine under forced water-cooling conditions.

To verify the 1D-SHC model, experiments with temperature rising and various fluid inlet velocities of the no-load machine at the rated speed of 1000 r/min were conducted, as shown in Figure 20. It can be seen that when the inlet velocity was bigger than 1.1 m/s, the temperature of the equivalent stator core decreased slowly, which agrees with the simulations giving both 1D-SHC and CFD results.

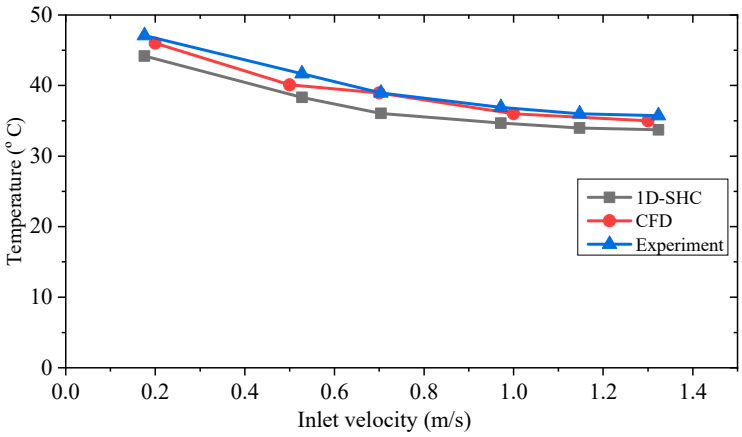

Figure 20. The equivalent stator core temperatures in the 1D-SHC model, CFD model, and experiment.

Overall, satisfactory agreement was achieved between the calculation and measured results, considering manufacturing and testing tolerances.

6. Conclusions

In this paper, a LPTN model is constructed to predict transient thermal behavior of the FSPM machine. Meanwhile, a simplified 1D-SHC model is also proposed to obtain the relationship between the internal temperature of the stator and the coolant flow rate and coolant temperature. The time consumption of the LPTN and 1D-SHC models was significantly less than that of the CFD model, which has advantages in machine design and optimization with large amounts of data. Based on the housing water jacket cooling FSPM machine studied in this manuscript, the LPTN and 1D-SHC methods have accelerated the steady-state temperature calculation speed by 330 and 1100 times, respectively, compared to the CFD method, and have accelerated the transient calculation speed by 857 and 4285 times, respectively. The static and transient temperatures under different conditions were verified by the CFD calculations and experiments. The predicted results from the models agree well with experimental results. This work will be useful in further investigation of thermal analysis of FSPM machines.

Author Contributions: Conceptualization, W.H.; methodology, W.Y. and Z.W.; software, W.Y.; investigation, W.Y. All authors have read and agreed to the published version of the manuscript.

Funding: This research was funded by the National Science Fund for Distinguished Young Scholars of China under Grant 51825701 and the Major Program of National Natural Science Foundation of China under Grant 51991381.

Data Availability Statement: The data presented in this study are available on request from the corresponding author. The data are not publicly available due to the project being still in progress.

Conflicts of Interest: The authors declare no conflict of interest.

References

1. Liu, C.; Chau, K.T.; Lee, C.H.T.; Song, Z. A critical review of advanced electric machines and control strategies for electric vehicles. *Proc. IEEE* **2021**, *109*, 1004–1028. [CrossRef]
2. Lee, C.H.T.; Hua, W.; Long, T.; Jiang, C.; Iyer, L.V. A critical review of emerging technologies for electric and hybrid vehicles. *IEEE Open, J. Veh. Technol.* **2021**, *2*, 471–485. [CrossRef]

3. Husain, I.; Ozpineci, B.; Islam, M.S.; Gurpinar, E.; Su, G.; Yu, W.; Chowdhury, S.; Xue, L.; Rahman, D.; Sahu, R. Electric Drive Technology Trends, Challenges, and Opportunities for Future Electric Vehicles. *Proc. IEEE* **2021**, *109*, 1039–1059. [CrossRef]
4. Wang, P.; Hua, W.; Zhang, G.; Wang, B.; Cheng, M. Principle of flux-switching PM machine by magnetic field modulation theory part II: Electromagnetic torque generation. *IEEE Trans. Ind. Electron.* **2022**, *69*, 2437–2446. [CrossRef]
5. Sheng, Z.; Wang, D.; Fu, J.; Hu, J. A computationally efficient spatial online temperature prediction method for PM machines. *IEEE Trans. Ind. Electron.* **2022**, *69*, 10904–10914. [CrossRef]
6. Cao, L.; Fan, X.; Li, D.; Kong, W.; Qu, R.; Liu, Z. Improved LPTN-based online temperature prediction of permanent magnet machines by global parameter identification. *IEEE Trans. Ind. Electron.* **2023**, *70*, 8830–8841. [CrossRef]
7. Zhang, H.; Giangrande, P.; Sala, G.; Xu, Z.; Hua, W.; Madonna, V.; Gerada, D.; Gerada, C. Thermal model approach to multisector three-phase electrical machines. *IEEE Trans. Ind. Electron.* **2021**, *68*, 2919–2930. [CrossRef]
8. Hwang, S.W.; Ryu, J.Y.; Chin, J.W.; Park, S.H.; Kim, D.K.; Lim, M.S. Coupled electromagnetic-thermal analysis for predicting traction motor characteristics according to electric vehicle driving cycle. *IEEE Trans. Veh. Technol.* **2021**, *70*, 4262–4272. [CrossRef]
9. Paar, C.; Muetze, A. Influence of dry clutch and ICE transmission integration on the thermal load of a PM based integrated starter-generator. In Proceedings of the IEEE Energy Conversion Congress and Exposition (ECCE), Montreal, QC, Canada, 20–24 September 2015; pp. 106–111.
10. Zhang, G.; Hua, W.; Cheng, M.; Zhang, B.; Guo, X. Coupled magnetic-thermal fields analysis of water cooling flux-switching permanent magnet motors by an axially segmented model. *IEEE Trans. Magn.* **2017**, *53*, 8106504. [CrossRef]
11. Du, J.; Liu, Q.; Xue, Y.; Wang, S. Fast Thermal analysis of an ISG in hybrid electric vehicle drive system. In Proceedings of the International Conference on Electrical Machines and Systems (ICEMS), Sydney, NSW, Australia, 11–14 August 2017; pp. 1–6.
12. Nachouane, A.B.; Abdelli, A.; Friedrich, G.; Vivier, S. Numerical Study of Convective Heat Transfer in the End Regions of a Totally Enclosed Permanent Magnet Synchronous Machine. *IEEE Trans. Ind. Appl.* **2017**, *53*, 3538–3547. [CrossRef]
13. Assaad, B.; Benkara, K.E.; Vivier, S.; Friedrich, G.; Michon, A. Thermal design optimization of electric machines using a global sensitivity analysis. *IEEE Trans. Ind. Appl.* **2017**, *53*, 5365–5372. [CrossRef]
14. Li, R.; Cheng, P.; Lan, H.; Ren, Y.; Hong, Y. Analytic Guided Magnetic-Thermal Kriging Surrogate Model and Multi-Objective Optimization of Synchronous Generator. In Proceedings of the IECON 2022—48th Annual Conference of the IEEE Industrial Electronics Society, Brussels, Belgium, 17–20 October 2022; pp. 1–6.
15. Bertotti, G. General properties of power losses in soft ferromagnetic materials. *IEEE Trans. Magn.* **1987**, *24*, 621–630. [CrossRef]
16. Zhu, S.; Cheng, M.; Dong, J.; Du, J. Core loss analysis and calculation of stator permanent-magnet machine considering DC-biased magnetic induction. *IEEE Trans. Ind. Electron.* **2014**, *61*, 5203–5212. [CrossRef]
17. Yamazaki, K. Torque and efficiency calculation of an interior permanent magnet motor considering harmonic iron losses of both the stator and rotor. *IEEE Trans. Magn.* **2003**, *39*, 1460–1463. [CrossRef]
18. Sadowski, N.; Lajoie-Mazenc, M.; Bastos, J.P.A.; Ferreira da Luz, M.V.; Kuo-Peng, P. Evaluation and analysis of iron losses in electrical machines using the rain-flow method. *IEEE Trans. Magn.* **2000**, *36*, 1923–1926. [CrossRef]
19. Simao, C.; Sadowski, N.; Batistela, N.J.; Bastos, J.P.A. Evaluation of hysteresis losses in iron sheets under DC-biased inductions. *IEEE Trans. Magn.* **2009**, *45*, 1158–1161. [CrossRef]
20. Yu, W.; Hua, W.; Wang, P.; Tang, C.; Zhang, G.; Cao, R. Coupled electromagnetic-thermal analysis of a 130 kW interior-PM machine for electric vehicles based on field-circuit coupling method. In Proceedings of the International Conference on Electrical Machines and Systems (ICEMS), Harbin, China, 11–14 August 2019; pp. 1–5.
21. Chen, S. *The Design of Motors*; China Machines Press: Beijing, China, 2000; pp. 94–95.
22. Li, H.; Shen, Y. Thermal analysis of the permanent-magnet spherical motor. *IEEE Trans. Energy Convers.* **2015**, *30*, 991–998. [CrossRef]
23. Mellor, P.H.; Roberts, D.; Turner, D.R. Lumped parameter thermal model for electrical machines of TEFC design. *IEE Proc. B-Electr. Power Appl.* **1991**, *138*, 205–218. [CrossRef]
24. Sciascera, C.; Giangrande, P.; Papini, L.; Gerada, C.; Galea, M. Analytical thermal model for fast stator winding temperature prediction. *IEEE Trans. Ind. Electron.* **2017**, *64*, 6116–6126. [CrossRef]
25. Ahmed, F.; Ghosh, E.; Kar, N.C. Transient thermal analysis of a copper rotor induction motor using a lumped parameter temperature network model. In Proceedings of the IEEE Transportation Electrification Conference and Expo (ITEC), Dearborn, MI, USA, 27–29 June 2016; pp. 1–6.
26. Yunus, A.C. *Heat and Mass Transfer: A Practical Approach*; McGraw-Hill: New York, NY, USA, 2007; pp. 133–137, 150–159, 410–411, 482–490, 517–521.
27. Chen, M.; Hua, W.; Zhao, G. Thermal performance of a flux-switching permanent magnet machine for an integrated starter generator in hybrid electric vehicles. In Proceedings of the International Conference on Electrical Machines and Systems (ICEMS), Sydney, NSW, Australia, 11–14 August 2017; pp. 1–6.